ARTICLE

Hierarchical porous nitrogen-rich carbon monoliths *via* ice-templating: high capacity and high-rate performance as lithium-ion battery anode materials

Aled D. Roberts[a,b], Suxi Wang[b], Xu Li[b*], and Haifei Zhang[a]*

Hierarchical porous nitrogen-rich carbon monoliths were prepared from a polyacrylonitrile (PAN) precursor by employing a novel & facile ice-templating, thermal annealing and pyrolysis technique. The achieved carbon monoliths were characterised by scanning electron microscopy (SEM), Hg-intrusion porosimetry, thermogravimetric analysis (TGA), N_2 gas-sorption, elemental analysis, X-ray photoelectron spectroscopy (XPS), powder X-ray diffraction (XRD) and Raman spectroscopy. Electrochemical evaluation of the carbon materials as anodes for the rechargeable lithium-ion battery revealed an impressive stable reversible capacity as high as 745 mAh g^{-1} at a current density of 50 mA g^{-1}. Incorporation of melamine (for further N-doping) and graphene into the carbon monoliths was achieved easily, and found to significantly enhance high rate performance – with a reversible capacity of about 300 mAh g^{-1} obtained at the ultra high current density of 10 A g^{-1}.

1. Introduction

In order to reduce CO_2 emissions and thereby mitigate climate change, advanced energy storage systems are required for green technologies such as electric vehicles and renewable energy load-levelling.[1-3] The rechargeable (or *secondary*) lithium-ion battery (LIB) is amongst the most advanced electrochemical energy storage systems at present, having many advantages over alternative battery technologies; such as a relatively high energy density and operating voltage, long lifespan and a flexible and lightweight design.[4] The current generation of LIBs have a number of limitations however, which includes a limited specific capacity (372 mAh g^{-1}) and power density of the graphite-based anode.[4, 5] In order to overcome these shortcomings and develop a new generation of advanced LIBs, new materials with fundamentally higher capacities and power densities need to be developed.[6]

There has been much interest recently in the development of novel carbon-based nanomaterials to replace graphite as the anode material of choice in the current generation of LIBs. Such nanomaterials have included graphene,[7] carbon nanotubes,[8] carbon spheres,[9, 10] porous monoliths,[10-12] and carbon nanofiberes (CNFs).[13-16] 3D porous carbon structures, fabricated *via* so-called templating processes, often display superior anode performance over alternative forms of carbon, particularly in regard to specific capacity and high rate performance.[11, 12] In particular, it has been shown that carbon structures with porosity spanning the macro-, meso- and micro-pore size domains (so-called *hierarchical* porosity) display even superior performance, particularly at high current rates. The superior performance of such hierarchical networks can be attributed to efficient Li ion diffusion within the network of transport pathways – enhancing Li ion diffusion kinetics which would typically be the rate limiting step at high current densities.[17]

Typical templates which may be used to direct the structure of the porous carbon can be categorized as either 'hard' (inorganic), or 'soft' (organic) materials.[10, 11] The synthesis, assembly and subsequent removal of such sacrificial templates (*e.g.* treatment with HF or conc. NaOH to remove silica-based templates), are significant shortcomings of these procedures, and would likely restrict the commercialization of the resultant porous carbons due to high costs and complexity of the processes.[10, 11] Recently however, there has been a focus on the development of relatively facile templating techniques for the fabrication of porous carbons.[11] Utilizing ice crystals (*ice-templating*) to direct the formation of a porous precursor material (typically a polymer), which is then subsequently converted to carbon *via* pyrolysis, can be regarded as a relatively facile procedure for the fabrication of porous carbons.[10] Nishihara *et al.* crosslinked an aqueous solution of resorcinol-formaldehyde (RF) to form a hydrogel network prior to the ice-templating process. After carbonization, microhoneycomb porous carbons with Brunauer-Emmett-Teller

(BET) surface areas up to 1280 m^2 g^{-1} were obtained.[18] An ice-templating method has also been employed to fabricate lignin nanofibers, which were subsequently converted to carbon *via* pyrolysis.[19] The naturally crosslinked nature of lignin likely helped maintain the structure upon heat treatment, and the resultant carbon nanofibers had a high BET surface area of about 1250 m^2 g^{-1}. Another recent example of the employment of ice-templating in the fabrication of a porous carbon was presented by Estevez *et al.*[20] Here they fabricated hierarchically porous carbons by combining ice-templating with hard-templating (employing colloidal silica as the hard templates) and physical activation with CO_2 to obtain high specific surface area carbons (up to 2000 m^2 g^{-1}) which showed impressive performance as CO_2 sorbents and as supercapacitor electrode materials.

Although PAN is a desirable carbon precursor – used extensively in the manufacture of carbon nanofibers – due to desirable properties such as high carbon yield, favourable mechanical properties and good thermal stability, it is rarely used as a precursor for templated porous carbons *via* traditional 'hard' or 'soft' templating procedures. This is primarily due to the fact that its low polarity and relatively high MW hinders diffusion into the template pores, leading to poor filling and hence a defective carbon structure.[21] Okada *et al.* recently developed a method in which porous PAN monoliths could be obtained *via* a thermally induced phase separation (TIPS) approach, avoiding the use of such templates.[22] Thermal annealing, carbonization and activation of the monoliths gave porous carbons which displayed high uptake of CO_2 under ambient conditions.[23]

In this paper we describe a method in which *aligned*-porous, nitrogen-rich carbon monoliths can be fabricated from commercially obtained PAN *via* a relatively simple ice-templating process, followed by thermal annealing and carbonization (Figure 1). Removal of the solvent crystals is achieved by lyophilisation (*freeze-drying*) or solvent exchange with H_2O, avoiding harsh chemical treatments required by other templating processes. Additives such as melamine, graphene, metal salts and/or nanoparticles can be easily dissolved or suspended in the initial PAN solutions to ultimately form composite materials. Thermal annealing of the porous PAN monoliths induces cross-linking and stabilization of the structure, preventing possible loss of the porous structure upon carbonization. When tested as anode materials for the LIB, an impressive initial reversible capacity of 745 mAh g^{-1} was obtained at a current density of 50 mA g^{-1}, which is twice as high as the theoretical specific capacity for graphite (372 mAh g^{-1}). Moreover, it was found that the incorporation of melamine (for *further* N-doping), and graphene would considerably improve the high-rate performance of the materials: with reversible capacities of about 200 and 250 mAh g^{-1} obtained at the ultra-high current density of 10 A g^{-1}, respectively. Co-doping with both melamine and graphene gave even better high rate performance; with a reversible capacity of about 300 mAh g^{-1} displayed at a current density of 10 A g^{-1}.
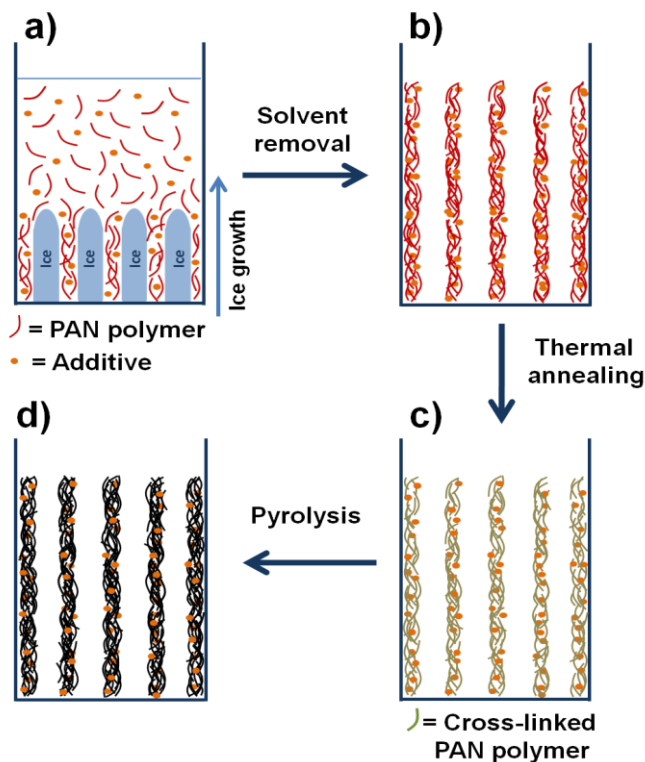

Figure 1. Schematic representation of the process in which the ice-templated PAN-derived porous carbons are prepared. a) directional freezing of PAN-based solution, b) solvent removal to give ice-templated porous polymer by freeze-drying or solvent exchange, c) thermal annealing to cross-link the structure, d) pyrolysis to produce the templated porous carbon.

2. Experimental

2.1 Materials

Polyacrylonitrile (PAN, MW 150,000), poly(sodium 4-styrenesulfonate) (PSS, MW 70,000), melamine (99 %) and hydrazine hydrate (40% aqueous solution) were purchased from Sigma Aldrich and used without further purification. An aqueous graphene oxide suspension (5 mg cm^{-3}) was purchased from Graphene Supermarket® and used as supplied. Standard analytical grade solvents and deionised water were used routinely.

2.2 Sample preparation

Preparation of the carbon monolith from PAN

PAN (5 g) was dissolved into dimethyl sulfoxide (DMSO) (100 cm^3) under stirring at 60 °C. 1.5 cm^3 of the cool solution was then transferred to a 10 mm x 75 mm borosilicate glass test tube (Fischer Scientific) and immersed into a bath of liquid nitrogen at a rate of about 5 mm min^{-1}. To remove the frozen DMSO crystals, the sample was either subject to lyophilisation for 48 h using a Virtis Advantage Benchtop Freeze Drier. Alternatively, the frozen samples could be immersed in ice-cold water

overnight to remove the DMSO crystals *via* solvent exchange - the water being subsequently removed by vacuum drying at 60 °C for *ca.* 3h. *For consistence*, all the samples reported in this study were prepared by the freeze-drying approach. The ice-templated macroporous PAN monolith was denoted as PANn, where n is the PAN concentration in DMSO in mg cm^{-3}.

The ice-templated porous PAN monolith was firstly subject to oxidative annealing by heating in a Carbolite CWF 1200 chamber furnace in air to a temperature of 280 °C at a rate of 1 °C min^{-1}, before being held at that temperature for 1 h. After cooling naturally to room temperature, the annealed PAN monolith was then pyrolysed by heating under an Ar atmosphere to a temperature of 800 °C at a rate of 5 °C min^{-1}, before being held at that temperature for 2.5 h. This was done in the furnace fitted with a gas line and a steel pyrolysis chamber ('home-made' set up, schematically represented in Figure S1). The hierarchical porous carbon monolith was denoted as CPANn, where n is the PAN concentration in DMSO in mg cm^{-3}.

Preparation of melamine-doped carbon monolith

PAN (5 g) and melamine (0.75 g) were dissolved into DMSO (100 cm^3) under stirring at 60 °C. The abovementioned procedure for the preparation of the CPAN monolith was then followed to give the melamine-doped CPAN50 monolith.

Preparation of graphene-doped carbon monolith

Preparation of aqueous graphene suspension:

A PSS-stabilized aqueous graphene dispersion was prepared following a modified procedure described in the literature.[24] Initially 3 g of PSS was dissolved in 20 cm^3 of deionized water under stirring at room temperature for 2 hours. 10 cm^3 of a commercially obtained aqueous graphene oxide solution (5 mg cm^{-3}) was then added, and the mixture was sonicated for *ca.* 30 min. 2 cm^3 of 40 % hydrazine hydrate was then added before the mixture was refluxed at 130 °C for 24 h. After cooling to room temperature, the suspension was washed by subjecting to 3 cycles of centrifuging and re-dispersion in deionized water. After the final wash, the graphene was re-dispersed with deionized water to make up to a concentration of 3.3 mg cm^{-3}. This suspension was then sonicated for a further 10 minutes. Determination of the sulphur content *via* elemental analysis revealed a PSS:graphene ratio of approximately 1:1.

Preparation of composite:

PAN (5 g) was dissolved into DMSO (100 cm^3) under stirring at 60 °C. 5 cm^3 of the above-prepared 3.3 mg cm^{-3} aqueous graphene solution was then added, and the stirring was continued for *ca.* 1 h in order to obtain a homogenous dispersion. The abovementioned procedure for the preparation of the carbon monolith was then followed to give the graphene-doped carbon monolith.

Preparation of melamine- *and* graphene- doped carbon monolith

PAN (5 g) and melamine (0.75 g) were dissolved into DMSO (100 cm^3) under stirring at 60 °C. 5 cm^3 of the above-prepared 3.3 mg cm^{-3} aqueous graphene solution was then added, and the stirring was continued for *ca.* 1 h in order to obtain a homogenous dispersion. The abovementioned procedure for the preparation of the carbon monolith was then followed to give the melamine- *and* graphene- doped carbon monolith.

2.3 Characterization

Surface areas and micro- and meso- pore size distributions were measured by nitrogen sorption at 77 K using a Micromiretics ASAP 2420 volumetric absorption analyser. The samples were degassed at 150 °C overnight before analysis. Macropore size-distributions (up to 200 μm) were measured by Hg intrusion porosimetry using a Micromiretics Autopore IV 9500 porosimeter. Powder X-ray diffraction (XRD) analysis was performed using a PANanalytical X'Pert PRO HTS X-ray diffractometer. Raman spectra were recorded using a Renishaw inVia Raman microscope fitted with a 633 nm laser, calibrated against a silicon wafer reference. Sample micromorphology was studied *via* scanning electron microscopy (SEM) using a Hitachi S-4800 SEM, with non-conductive samples initially coated with Au using an Emitech K550X Automated Sputter Coater. Thermogravimetric analysis (TGA) was carried out using a Q5000IR TGA; the samples were heated to 800 °C at a rate of 5 °C min^{-1} under an N_2 atmosphere. Conductivity measurements were taken *via* a two-probe method using a Keithley 2600A sourcemeter. Elemental analysis data was obtained from a Thermo FlashEA 1112 series CHNSO elemental analyser using the Microanalytical service at the University of Liverpool. The surface chemistry of the samples was studied on a VG ESCA LAB-220i XL X-ray photoelectron spectrometer (XPS) with an exciting source of Al.

2.4 Electrochemical evaluation

The electrochemical performance of the carbon monoliths were evaluated as anode in lithium-ion batteries after being grinded to powders. The working electrode was fabricated by coating the slurry of the carbon sample (80 wt %), Super-P (Timcal, 10 wt %), and polyvinylidene fluoride (PVDF) (10 wt %) in N-methyl pyrrolidinone (NMP) onto a copper foil. The coated copper foil was dried under vacuum at 120 °C overnight and then assembled into 2032 button cells in an argon-filled glove box with lithium foil, Celgard 2325 membrane and 1 M LiPF$_6$ in ethylene carbonate / dimethyl carbonate (1:1 v/v ratio) as the counter electrode, separator and electrolyte, respectively. The charge-discharge testing was conducted on NEWARE battery tester at different current densities with a cutoff voltage window of 0.005−3.0 V. The cyclic voltammetry (CV) tests were performed on an electrochemical workstation

(PGSTAT302, Autolab) within a voltage window of 0–3.0 V and at a scan rate of 0.01 mV s^{-1}.

3. Results and discussion

3.1 Preparation of hierarchical porous PAN monoliths

The preparation of the PAN-derived ice-templated porous carbons is illustrated in Figure 1. Firstly, PAN was dissolved in DMSO with concentrations ranging between 1 and 250 mg cm^{-3}. The solutions were then subject to directional freezing by slow submersion into a bath of liquid N$_2$ (-196 °C), before being subject to lyophilisation in order to remove the templating solvent crystals. DMSO was selected as a solvent due to its relatively low toxicity, high solubility towards PAN, and for the fact it has a high melting point (around 19 °C) making it convenient for freeze-drying. After DMSO crystal template removal through freeze drying, it was observed that the porous PAN monoliths obtained displayed no significant
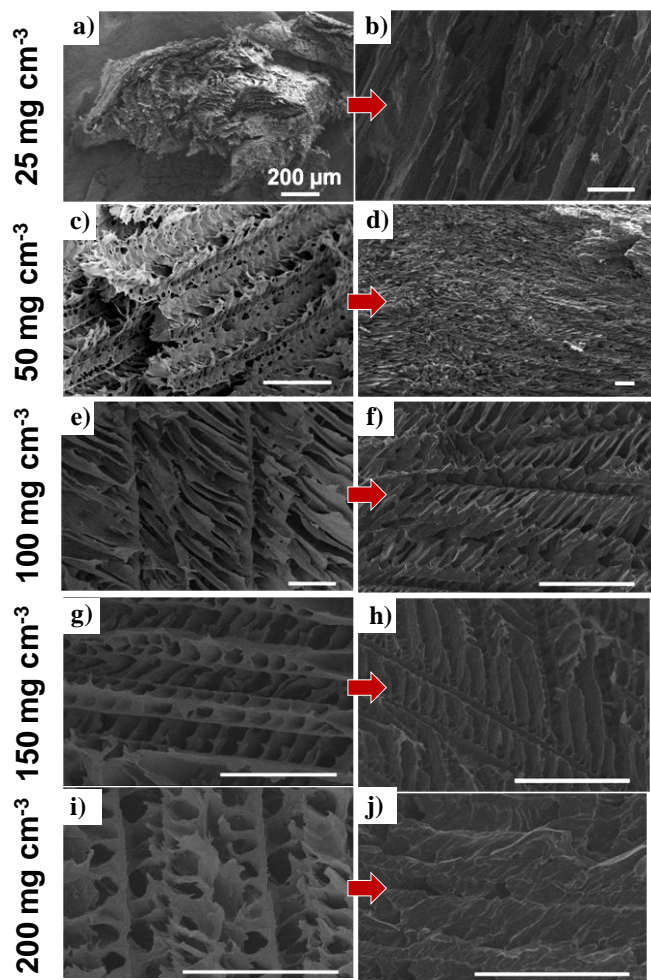

Figure 2. SEM images of the PAN monoliths from different initial PAN in DMSO concentrations before (a, c, e, g and i) and after (b, d, f, h, and j) pyrolysis. The scale bar represents 50 µm unless otherwise stated.

volumetric shrinkage. The monoliths formed from relatively low concentrations of PAN (< 10 mg cm^{-3}) had relatively poor mechanical stability and could easily be crushed between fingers; whereas structures formed from higher PAN concentration solutions were much stronger and could be handled easily without damaging. SEM analysis revealed that the PAN monoliths prepared from the relatively low concentrations were fibrous in nature, with no aligned microchannels, giving explanation to their relatively fragile nature (Figure S2). The relatively robust PAN monoliths prepared from higher PAN concentrations had an aligned morphology, with microchannels oriented along the path of the advancing solvent crystals in accordance with ice-templating theory (Figure 2).[25, 26] The microchannel size, judged by SEM, varied between 2 and 50 µm, which is consistent with other ice-templated porous materials described in the literature.[27-29]

3.2 Stabilization and pyrolysis of the porous PAN monoliths

In order to preserve the porous structure upon pyrolysis, the PAN monoliths were firstly processed by oxidative annealing by heating to 280 °C in air. This procedure is commonly applied in the manufacture of PAN derived CNFs to induce cyclization, dehydration, aromatization and crosslinking of the polymer backbone: resulting in a stable ladder-type structure (Figure S3).[30] After annealing, the PAN monoliths were then subject to carbonization at 800 °C under an Ar atmosphere. SEM imaging confirmed the retention of the macroporous structure after carbonization (Figure 2); although volumetric shrinkage of the monoliths of about 60 % was observed, along with cracking in some instances. Mercury intrusion porosimetry (MIP) was employed to quantify the pore characteristics before and after pyrolysis (Figure 3a). Here a PAN monolith, prepared from a PAN in DMSO solution with concentration of 50 mg cm^{-3} (denoted PAN50), was selected as a representative sample and analysed. It was found that the intrusion volume was reduced by 86%, with the total pore area shrunk by 77 % and the average pore diameter by 38 % (Table S1). TGA was also employed to investigate the mass loss during carbonization of PAN50. This revealed a mass loss of about 25% on heating to 280 °C (annealing temperature), before a further loss of about 40 % upon carbonization at 800 °C (Figure 3b).

3.3 Characterization of the CPAN materials

XRD and Raman spectroscopy were performed on the carbonized PAN50 monolith (denoted CPAN50) as a representative sample in order to investigate the microstructure of the materials. XRD measurements revealed two broad Bragg peaks at 2θ values of 25 and 43°, which were attributed to the (002) and (101) reflections of a turbostratic carbon structure (Figure 4a).[31] The approximate interlayer spacing of the graphite sheets (d$_{002}$) was calculated using the Bragg equation and found to be 3.55 Å. The mean crystallite size (L$_c$), calculated using the Scherrer equation, was found to be 2.21 nm – indicating an average of about 6.2 stacked graphene sheets in the c-plane per graphite crystallite.[32] First-order Raman
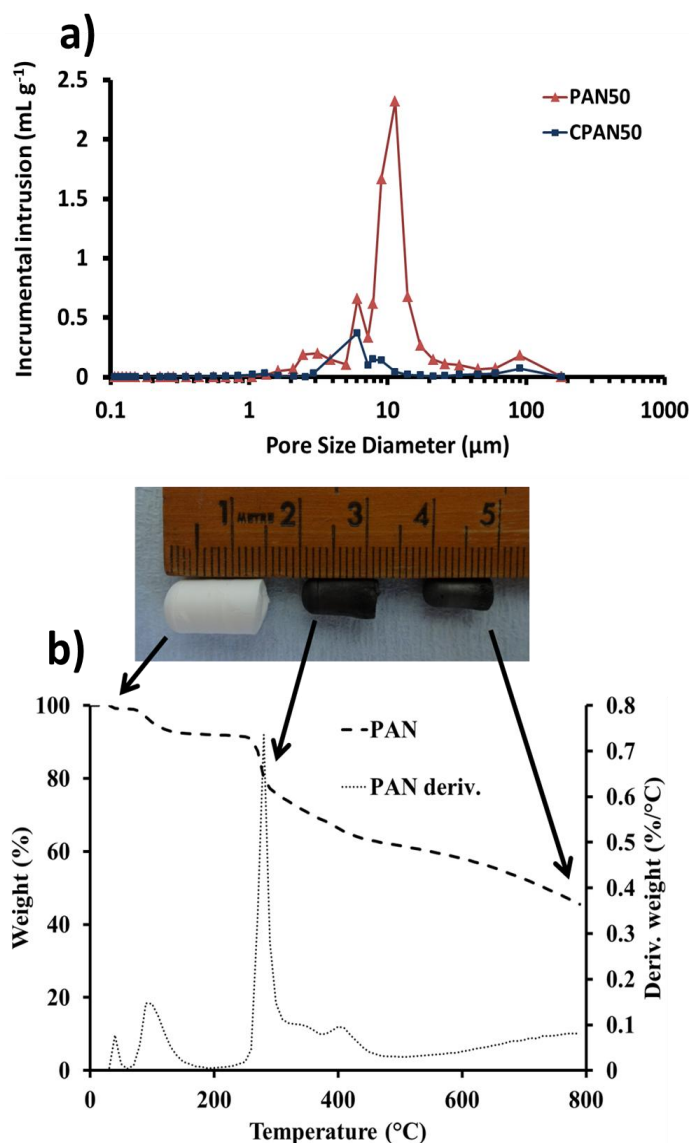
Figure 3. a) Macropore size distribution of the PAN50 monolith before and after carbonization (CPAN50). b) TGA of the PAN50 monolith undergoing carbonization.

spectroscopy of CPAN50 revealed two overlapping peaks at 1344 and 1580 cm^{-1} (Figure 4b); the former corresponding to the A_{1g} mode attributed to structural defects associated with a disordered carbon structure (D-band), and the latter corresponding to the E_{2g} mode associated with C=C stretching in graphitic carbon (G-band). The ratio of the intensity of D- and G-bands, I_D/I_G, was found to be 1.12 indicating a relatively disordered turbostratic carbon structure, concordant with the XRD measurements. The conductivity of the cylindrical monolithic samples was measured using a two-probe method, and found to be linear with respect to the initial PAN concentration in DMSO (Figure 4c). This linear relationship was simply attributed to the increased carbon density of the materials, leading to enhanced electron percolation and hence conductivity.
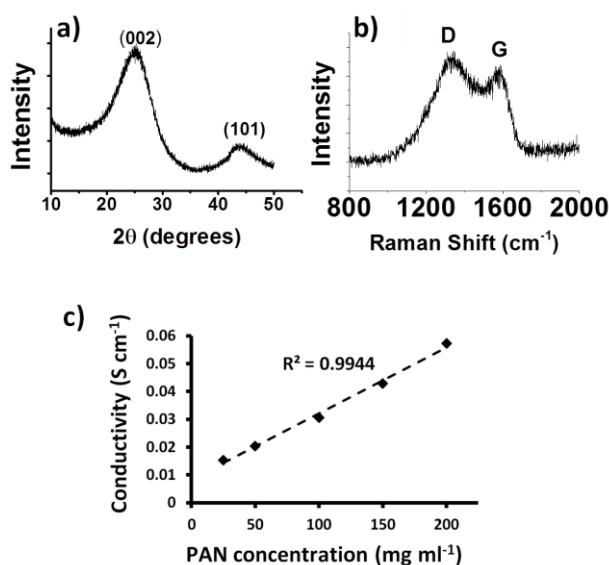

Figure 4. a) XRD and b) Raman spectrum of the CPAN50 monolith, and c) relationship between initial PAN concentration and electrical conductivity of the carbonized monoliths.

N_2 gas sorption was employed to investigate the pore characteristics of the representative CPAN50 material, from which a BET surface area of 173 m^2 g^{-1} was obtained (Figure 5a). The density functional theory (DFT) analysis suggested a bimodal distribution of micropores centred around 1.0 and 1.4 nm, whilst the Barrett-Joyner-Halenda (BJH) method calculated a broad distribution of mesopores (Figure 5b and 5c). The shape of the isotherm can be described roughly as type IV with a H4 hysteresis loop, displaying the phenomenon of low-pressure hysteresis (LPH) which has been observed for some other porous solids such as micro- and mesoporous silicas, microporous polymers, and activated carbons.[33-35] LPH has recently been suggested to be a consequence of incomplete degassing and insufficient pressure equilibration time.[33] However, even with a relatively high degassing temperature of 300 °C and long equilibration times (sample running time >1 week) LPH was still observed. This suggested that in this case the phenomenon could be due to entrapment of the gas molecules within the pores due to narrow openings and convoluted pore pathways, and/or swelling of the monoliths due to a non-rigid porous structure.[35, 36]

Elemental analysis of the CPAN materials was performed to determine the weight percentage of carbon, hydrogen, and nitrogen of the materials; with the remainder inferred to be oxygen introduced during the annealing step (Table S2). An interesting observation was the exceptionally high nitrogen content of the CPAN materials, found to be between about 15 and 17 % (Table S2); this is significantly higher than most other PAN-derived carbons described in the literature carbonized at similar temperatures – which typically have an N content of < 10 %.[37-39]
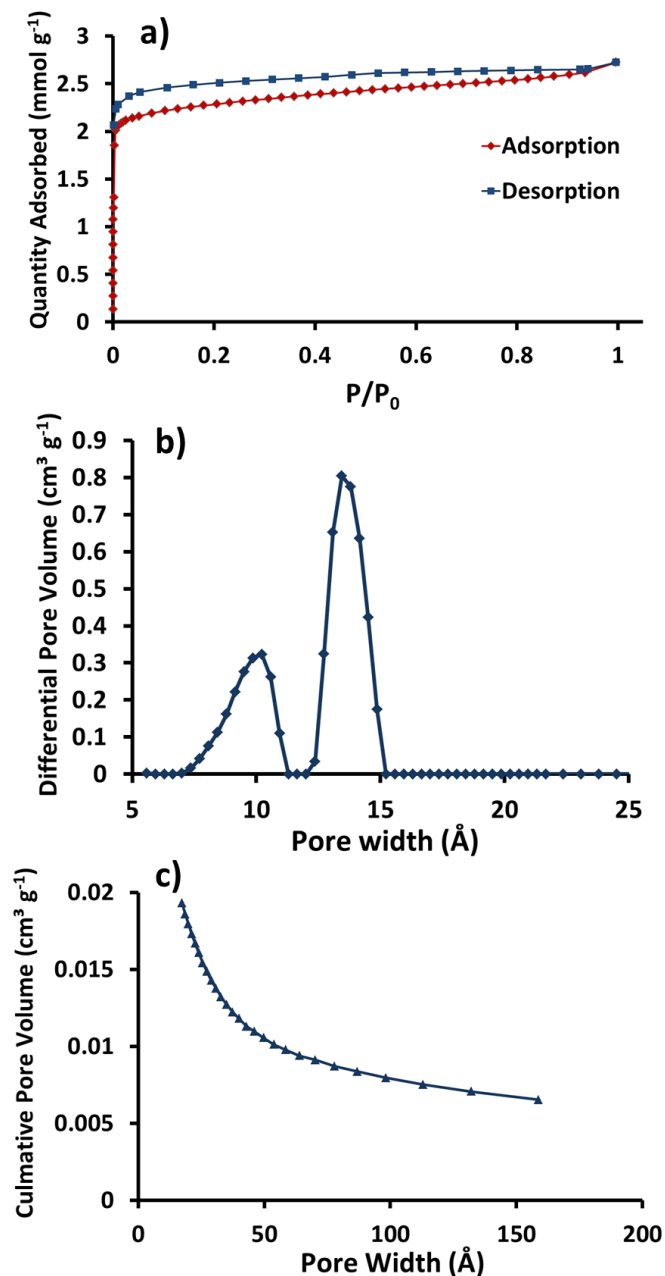
electrons, thereby contributing to the rate capability.[40, 43, 44] Although the Li storage mechanism in N-rich carbon is still unclear, it is believed to be related to the strong electronegativity of nitrogen and the hybridization of nitrogen lone pair electrons with the carbon π-orbitals, which makes for favorable binding sites for Li storage. In addition, the existence of N atoms also creates defects in the carbon and generates more active sites for the Li storage. Indeed numerous other repots have found that a high N-content can enhance the electrochemical profile of carbon-based electrode materials, particularly through an enhanced capacity and high-rate performance.[45-48] The origin of the remarkably high N-content within our materials is not clear. However, it is interesting to note that Okada *et al.* also reported a high N-content ($\sim$12 – 19 %) within their porous PAN-derived carbon monoliths, prepared *via* their thermally induced phase separation (TIPS) method.[23] It is hypothesised that in both our case and theirs, the porous monolith structure entraps nitrogen containing by-products of the pyrolysis process (such as NH_3 and HCN) resulting in a form of *self-doping*, giving the anomalously high N-content. Further studies would need to be performed to confirm this hypothesis however.
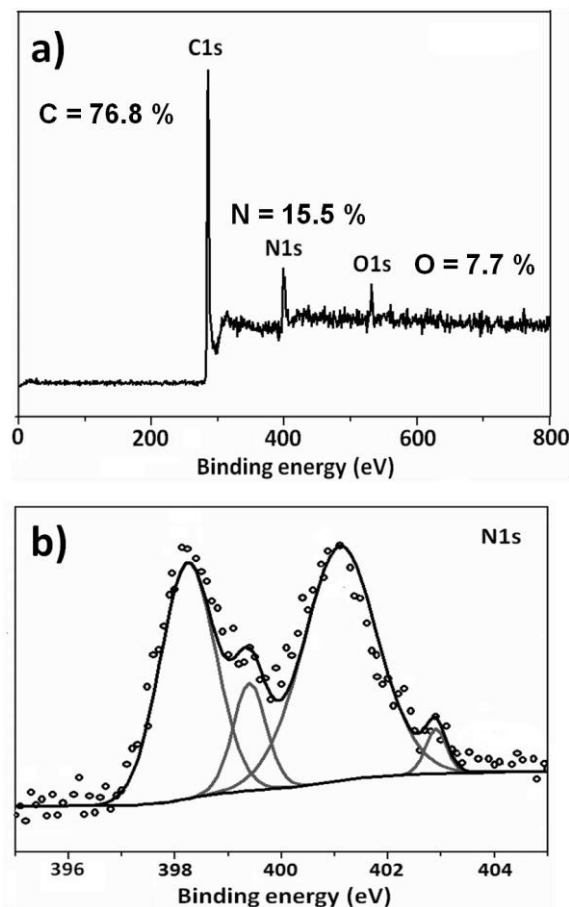

Figure 5. a) N_2 gas sorption isotherm, b) DFT pore size distribution and c) BJH pore size distribution of the CPAN50 monolith.

XPS analysis confirmed the high N-content; recording a value of 15.5 % for the CPAN25 material analysed as a representative sample (Figure 6). The N1s spectrum can be fitted into four component peaks located at 398.2, 399.4, 401.1 and 402.9 eV, which could be identified to pyridinic nitrogen (37.0 %), pyrrolic nitrogen (10.5 %), quaternary nitrogen (50.0 %) and oxidized nitrogen (2.5 %), respectively.[40, 41] As reported previously, only pentagonal pyrrolic nitrogen is formed at low temperature around 300 °C and it could be converted to pyridinic and quaternary nitrogen as the carbonization temperature rises.[40, 42] The quaternary nitrogen has been known to increase the electronic conductivity by generating excessive

Figure 6. a) XPS spectrum of the CPAN25 material, and b) closer view and peak fitting for the N1s spectrum.

3.4. Anode performance evaluation

Cyclic voltammetry (CV) of the CPAN25 material – selected as a representative as it had the highest reversible capacity (Figure S4) – displayed typical behaviour for a turbostratic porous carbon, with reductive intercalation of lithium occurring on the negative sweep as potentials approach 0 V relative to Li/Li+, and oxidative de-intercalation occurring on the positive sweep at similar potentials (Figure 7a). Constant current potentiometry (CCP), at a current density of 50 mA g^{-1}, revealed an initial
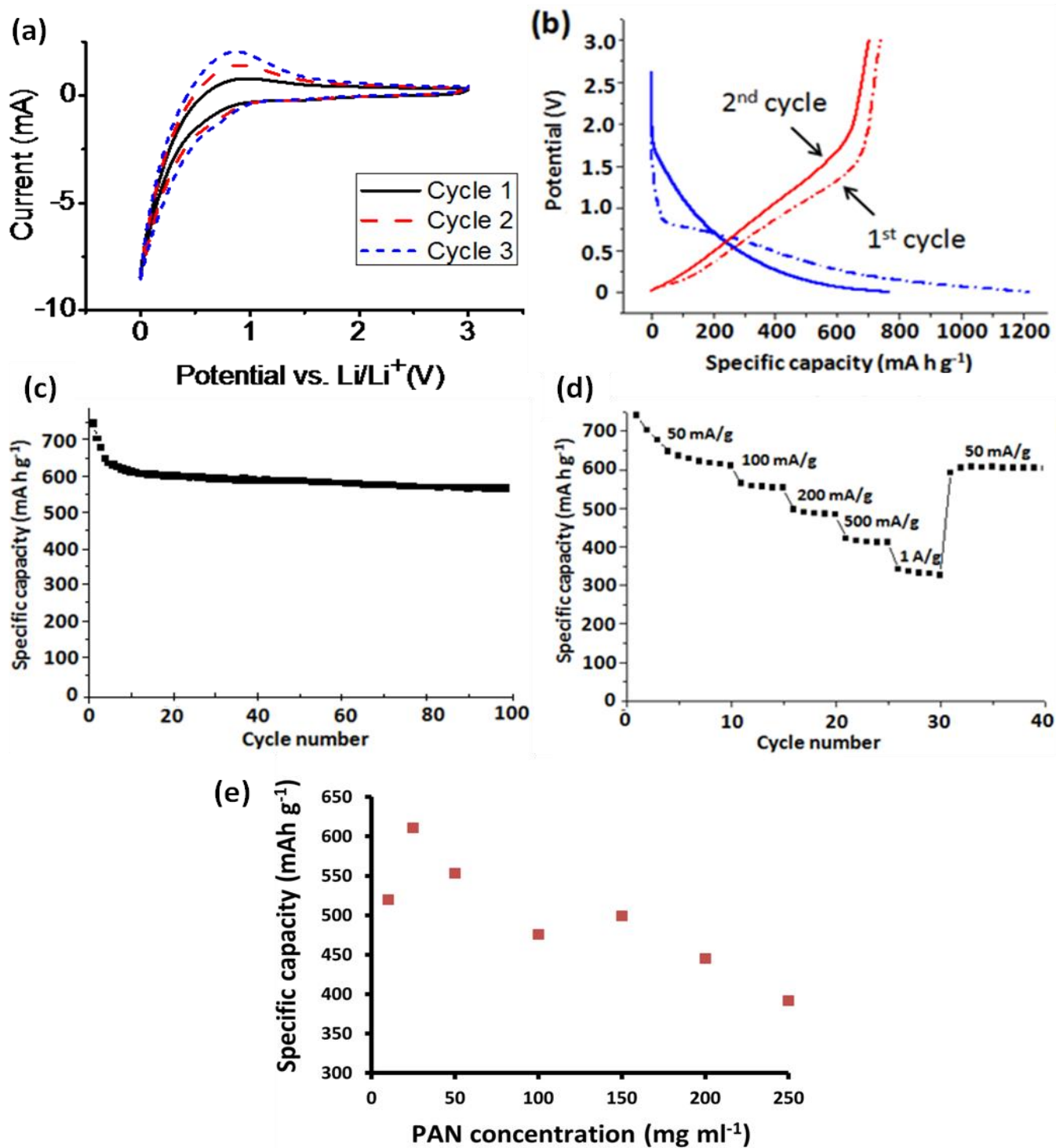

Figure 7. a) Cyclic voltammetry plot, b) constant current potentiometry profiles, and c) & d) charge-discharge profiles of the CPAN25 material. e) Specific capacity values after 10 cycles at 50 mA g^{-1} for the porous carbons prepared at different PAN concentrations.

irreversible capacity loss (C_{irr}) of 468 mAh g^{-1}, and a corresponding initial reversible capacity (C_{rev}) of 745 mAh g^{-1} (Figure 7b). This reversible capacity, which stabilized at about 611 mAh g^{-1} after 10 cycles, is substantially higher than the theoretical capacity for graphite (372 mAh g^{-1}). High cycle stability at this current density was also observed, with the specific capacity remaining above 560 mAh g^{-1} after 100 charge discharge cycles (Figure 7c). Good high-rate performance (figure 7d) was also observed, with a reversible capacity of about 320 mAh g^{-1} at a current density of 1 A g^{-1}. These factors compare favourably with that of other high-performance 'hard' or 'soft' templated porous carbons described in the literature (Table S3).[17, 32, 49] In particular, it should be noted that porous carbons which display high C_{rev} values also typically display a high C_{irr} too (between 650 – 2000 mAh g^{-1} based on a literature search), which isn't desirable from a practical point of view since a high C_{irr} reduces the overall capacity of a battery. A relatively high value for C_{irr} (hence low initial Coulombic efficiency) is observed in this study, which can be attributed to excessive formation of the solid electrolyte interphase (SEI) layer on the exposed surface of the materials. The SEI layer is associated with electrolyte decomposition and irreversible consumption of Li$^+$ ions. The approaches to reducing SEI and improving initial Coulombic efficiency may include the use of stable electrolytes and electrode materials with low surface area. However, there is a subtle balance between battery performance and SEI layer formation, which needs to be considered carefully.

We attribute the impressive anode performance of the materials to a number of factors. Firstly, the hierarchical porous structure provides efficient mass- and charge- transport pathways, allowing rapid Li ion diffusion to and from the electrode along with facile electron percolation. Moreover, the moderately high surface area permits a relatively large contact area for the electrode-electrolyte interface, facilitating rapid charge transfer, without being so high as to facilitate the excessive degradation of electrolyte and irreversible capacity loss through SEI formation. Other authors have also reported improved anode performance by employing such hierarchical porous structures; in particular those with high meso- and macro- pore volumes.[17, 45, 49, 50] The intrinsically high N-content is also believed to play an important role in the attainment of a relatively high capacity and good rate performance, as demonstrated by others.[45-47, 51, 52] For instance, Qie *et al.* recently fabricated carbon nanofiber webs with a high N-content (~16 %) which displayed an outstanding reversible capacity of 300 mAh g^{-1} at the ultra-high current density of 10 A g^{-1}.[47] N-rich porous carbons derived from proteins have also displayed a very impressive high rate performance of 210 mAh g^{-1} at a current density of 4 A g^{-1}.[45] It is interesting that the reversible capacity of the materials was found to be maximal with an initial PAN concentration of 25 mg cm^{-3} (CPAN25), with decreasing capacity at both higher and lower concentrations (Figure 7e). This trend of decreasing capacity at higher PAN concentrations can be attributed to the increased thickness of the walls of the carbon materials at higher PAN

concentrations, which may decrease the amount of accessible active material. The decrease in specific capacity at initial PAN
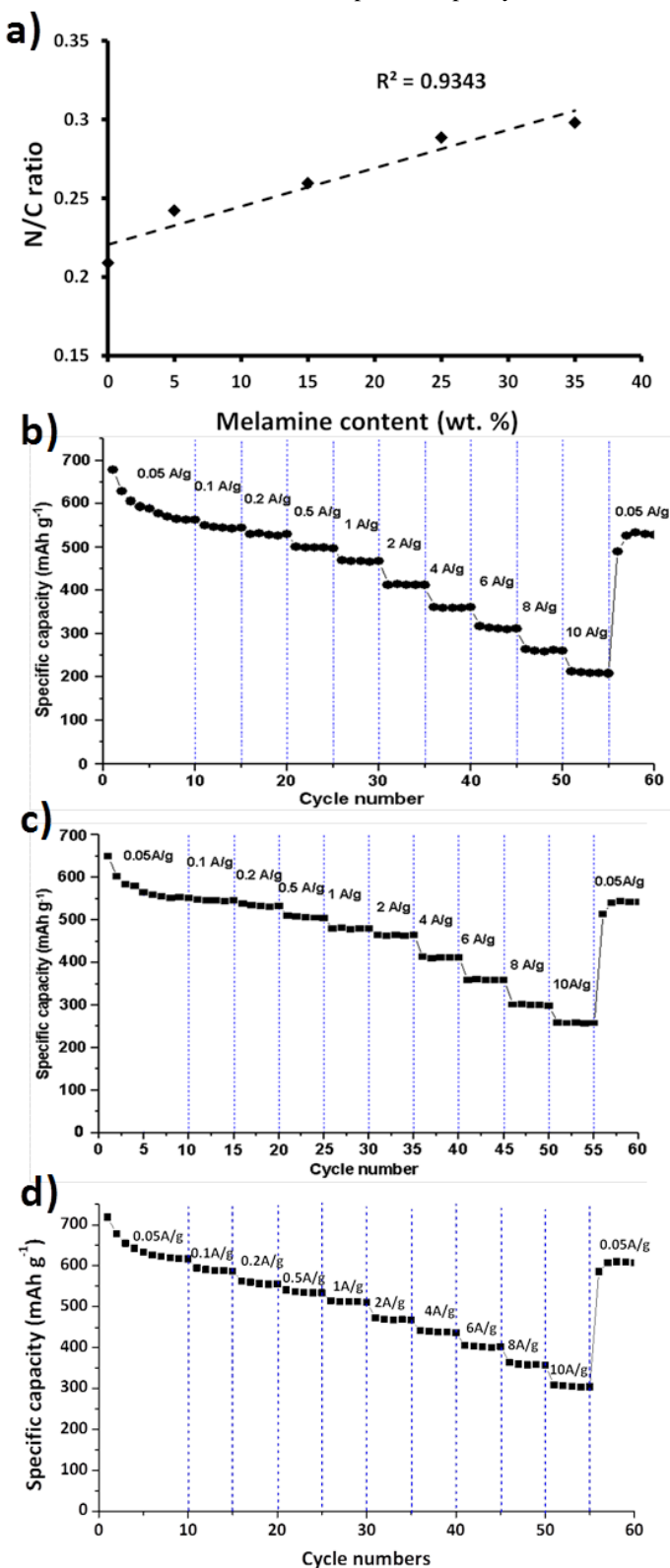
Figure 8. a) Relationship between N/C ratio and melamine content in initial PAN/DMSO solution. Rate performance of b) 15 wt% melamine-doped CPAN50, c) graphene-doped CPAN50, and d) graphene and melamine doped CPAN50.

concentrations below 25 mg cm^{-3} may be associated with the general change in morphology from an interconnected and aligned structure to a relatively disordered microfibrous structure, as was observed by SEM measurements (Figure 2). It is hypothesised that the capacity is relatively higher for an interconnected porous structure rather than a more fibrous structure due to facile electron and Li ion transport pathways, as suggested by Qie et al.[47]

3.5. Fabrication of CPAN-composite materials for improved electrochemical performance

Carbon materials have been intensively investigated to improve battery performance. For the ice-templating approach, it was found that simple dissolution or suspension of various substances within the initial PAN DMSO solutions, prior to directional freezing and freeze-drying, would lead to incorporation of such entities within the porous polymer. Subsequent carbonization would then lead to the incorporation of such substances within the final carbonaceous structure. For instance, commercially obtained silicon nanoparticles (<100 nm) were incorporated within the porous carbon this way (Figure S5), as was the metal salt Sn(OAc)$_2$ which was converted to SnO$_2$ during carbonization (Figure S6). The incorporation of melamine (for further N-doping) and graphene within the materials was also achieved, and was found to significantly enhance rate performance as detailed below.

3.5.1 CPAN-melamine composites for further N-doping

It has been reported that nitrogen-doping of carbonaceous LIB anode materials can lead to enhanced performance, particularly in regard to high-rate capability.[45-47, 51, 52] Further N-doping for the CPAN50 material was achieved by the simple incorporation of melamine within the initial PAN-DMSO solution; with a linear relationship between initial melamine concentration and resultant N-content observed by elemental analysis (Figure 8a). Electrochemical evaluation of a sample which contained 15 wt. % of melamine relative to PAN revealed a much improved high-rate performance; having a reversible capacity of about 200 mAh g^{-1} at an ultra-high current density of 10 A g^{-1} (Figure 8b).

3.5.2 CPAN-graphene composites

Since the discovery of its remarkable chemical, physical and electronic properties, graphene has attracted much interest in many fields including that of electrochemical energy storage.[7, 12, 51] Incorporation of graphene within the CPAN materials was achieved via simple dispersion of an aqueous PSS-stabilized, reduced graphene-oxide suspension into the PAN-DMSO solutions prior to directional freezing. Remarkably, even better high-rate performance than that of the N-doped system was achieved; with a reversible capacity of 250 mAh g^{-1} obtained at the current density of 10 A g^{-1} (Figure 8c) for the graphene-

doped CPAN50 system. The basis of the improved performance is not clear, however it is hypothesised that the high chemical diffusivity of lithium on a graphene plane (~10^{-7} – 10^{-6} cm^2 s^{-1}), in conjunction with the intrinsically high N-content and hierarchically porous structure of the electrode, serves to minimise internal resistances and rate-limiting kinetics within the electrode material. In doing so, high currents may be drawn from the electrode materials before rate-determining kinetics begin to hamper the electrode performance.[51, 53].

With improved high-rate performance for both the melamine- and graphene- doped CPAN materials, the effect of co-doping with both graphene and melamine was investigated. It was found that the high-rate performance for this system was improved still further, with a reversible capacity of about 300 mAh g^{-1} obtained at high current density of 10 A g^{-1} (Figure 8d) for the co-doped CPAN50 system. This is outstanding high-rate performance and on par with the best ultra-high rate performance carbon-based materials that could be found in the literature, despite the relative simplicity of the fabrication technique (Table S4).[17, 45, 47-52]

4. Conclusions

Hierarchically porous PAN-derived carbons, with an inherently high N-content, were prepared via a simple ice-templating and carbonization technique. Unlike many other templating processes, which employ relatively complex and costly techniques for the fabrication and subsequent removal of the templates, the solvent crystal templates are formed by simply freezing a polymer solution, and removed by a facile freeze-drying procedure. The achieved hierarchical porous carbon monoliths demonstrate outstanding specific capacity and high rate performance as LIB anode materials despite this relatively simple preparation process. The improved performance was attributed principally to these features: 1) a hierarchical structure of pores providing an efficient transport pathway for Li ions to be transported to and from the active electrode material, and 2) an exceptionally high N-content attributed to employing a N-rich precursor and the proposed self-doping mechanism. Moreover, incorporation of various entities within the porous carbons was achieved by simply dispersing the substances into the initial PAN-DMSO solution prior to the freezing step. The incorporation of melamine, to attain further N-doping, and graphene, both significantly enhanced high-rate performance, with a reversible capacity of 300 mAh g^{-1} achieved at the ultra-high current density of 10 A g^{-1} for the co-doped system - which is among the highest capacity performance for a carbon-based anode material reported to date.

Notes and references

[a] Department of Chemistry, University of Liverpool, Oxford Street, Liverpool, L69 7ZD, UK. Email: zhanghf@liv.ac.uk

[b] Institute of Materials Research and Engineering, A*STAR, Singapore 117602. Email: x-li@imre.a-star.edu.sg

1. P. G. Bruce, S. A. Freunberger, L. J. Hardwick and J.-M. Tarascon, *Nat. Mater.*, 2012, **11**, 19-29.
2. A. Simpson, *Cost-benefit analysis of plug-in hybrid electric vehicle technology*, National Renewable Energy Laboratory, 2006.
3. J. P. Barton and D. G. Infield, *Energy Conversion, IEEE Transactions on*, 2004, **19**, 441-448.
4. J. M. Tarascon and M. Armand, *Nature*, 2001, **414**, 359-367.
5. M. Endo, C. Kim, K. Nishimura, T. Fujino and K. Miyashita, *Carbon*, 2000, **38**, 183-197.
6. M. Armand and J. M. Tarascon, *Nature*, 2008, **451**, 652-657.
7. X. Huang, X. Qi, F. Boey and H. Zhang, *Chem. Soc. Rev.*, 2012, **41**, 666-686.
8. B. J. Landi, M. J. Ganter, C. D. Cress, R. A. DiLeo and R. P. Raffaelle, *Energy Environ. Sci.*, 2009, **2**, 638-654.
9. A. A. Deshmukh, S. D. Mhlanga and N. J. Coville, *Mater.Sci. Eng. R*, 2010, **70**, 1-28.
10. A. D. Roberts, X. Li and H. Zhang, *Chem. Soc. Rev.*, 2014, 43, 4341-4356.
11. H. Nishihara and T. Kyotani, *Adv. Mater.*, 2012, **24**, 4473-4498.
12. S. Han, D. Wu, S. Li, F. Zhang and X. Feng, *Adv. Mater.*, 2014, **26**, 849-864.
13. J. Kong, H. R. Tan, S. Y. Tan, F. Li, S. Y. Wong, X. Li and X. Lu, *Chem. Commun.*, 2010, **46**, 8773-8775.
14. J. Kong, S. Y. Wong, Y. Zhang, H. R. Tan, X. Li and X. Lu, *J. Mater. Chem.*, 2011, **21**, 15928-15934.
15. C. Zhu, X. Mu, P. A. van Aken, Y. Yu and J. Maier, *Angew. Chem. Int. Ed.*, 2014, **53**, 2152-2156.
16. L. Ji and X. Zhang, *Nanotechnology*, 2009, **20**, 155705.
17. Y. S. Hu, P. Adelhelm, B. M. Smarsly, S. Hore, M. Antonietti and J. Maier, *Adv. Funct. Mater.*, 2007, **17**, 1873-1878.
18. H. Nishihara, S. R. Mukai and H. Tamon, *Carbon*, 2004, **42**, 899-901.
19. J. Spender, A. L. Demers, X. Xie, A. E. Cline, M. A. Earle, L. D. Ellis and D. J. Neivandt, *Nano Lett.*, 2012, **12**, 3857-3860.
20. L. Estevez, R. Dua, N. Bhandari, A. Ramanujapuram, P. Wang and E. P. Giannelis, *Energy Environ. Sci.*, 2013, **6**, 1785-1790.
21. Q.-Y. Wu, L.-S. Wan and Z.-K. Xu, *Polymer*, 2013, **54**, 284-291.
22. K. Okada, M. Nandi, J. Maruyama, T. Oka, T. Tsujimoto, K. Kondoh and H. Uyama, *Chem. Commun.*, 2011, **47**, 7422-7424.
23. M. Nandi, K. Okada, A. Dutta, A. Bhaumik, J. Maruyama, D. Derks and H. Uyama, *Chem. Commun.*, 2012, **48**, 10283-10285.
24. S. Stankovich, R. D. Piner, X. Chen, N. Wu, S. T. Nguyen and R. S. Ruoff, *J. Mater. Chem.*, 2006, **16**, 155-158.
25. S. Nardecchia, D. Carriazo, M. L. Ferrer, M. C. Gutiérrez and F. del Monte, *Chem. Soc. Rev.*, 2013, **42**, 794-830.
26. L. Qian and H. Zhang, *J. Chem. Technol. Biotechnol.*, 2011, **86**, 172-184..
27. K. Katuri, M. L. Ferrer, M. C. Gutiérrez, R. Jiménez, F. del Monte and D. Leech, *Energy Environ. Sci.* 2011, **4**, 4201-4210.
28. D. Deville, *Adv. Eng. Mater.*, 2008, **10,** 155-169.
29. A. D. Roberts and H. Zhang, *Int. J. Pharm.*, 2013, **447**, 241-250.
30. M. S. A. Rahaman, A. F. Ismail and A. Mustafa, *Polym. Degrad. Stabil.*, 2007, **92**, 1421-1432.
31. S.-S. Tzeng and Y.-G. Chr, *Mater. Chem. Phys.*, 2002, **73**, 162-169.
32. H. Zhou, S. Zhu, M. Hibino, I. Honma and M. Ichihara, *Adv. Mater.*, 2003, **15**, 2107-2111.
33. A. M. Silvestre-Albero, J. M. Juárez-Galán, J. Silvestre-Albero and F. Rodríguez-Reinoso, *J. Phys. Chem. C*, 2012, **116**, 16652-16655.
34. W. J. Braida, J. J. Pignatello, Y. Lu, P. I. Ravikovitch, A. V. Neimark and B. Xing, *Environ. Sci. Technol.*, 2002, **37**, 409-417.
35. J. Jeromenok and J. Weber, *Langmuir*, 2013, **29**, 12982-12989.
36. M. Olivares-Marin, P. Palomino, J. M. Amarilla, E. Enciso and D. Tonti, *J. Mater. Chem. A*, 2013, **1**, 14270-14279.
37. X. Meng, H. Cui, J. Dong, J. Zheng, Y. Zhu, Z. Wang, J. Zhang, S. Jia, J. Zhao and Z. Zhu, *J. Mater. Chem. A*, 2013, **1**, 9469-9476.
38. E. J. Ra, E. Raymundo-Piñero, Y. H. Lee and F. Béguin, *Carbon*, 2009, **47**, 2984-2992.
39. B.-H. Kim and K. S. Yang, *Electrochim. Acta*, 2013, **88**, 597-603.
40. F. Su, C. K. Poh, J. S. Chen, G. Xu, D. Wang, Q. Li, J. Lin and X. W. Lou, *Energy Environ. Sci.*, 2011, **4**, 717-724.
41. X. Y. Chen, D. H. Xie, C. Chen and J. W. Liu, *J. Colloid Interface Sci.*, 2013, **393**, 241-248.
42. Z. Mou, X. Chen, Y. Du, X. Wang, P. Yang and S. Wang, *Appl. Surf. Sci.*, 2011, **258**, 1704-1710.
43. H. M. Jeong, J. W. Lee, W. H. Shin, Y. J. Choi, H. J. Shin, J. K. Kang and J. W. Choi, *Nano Lett.*, 2011, **11**, 2472-2477.
44. M. Seredych, D. Hulicova-Jurcakova, G. Q. Lu and T. J. Bandosz, *Carbon*, 2008, **46**, 1475-1488.
45. Z. Li, Z. Xu, X. Tan, H. Wang, C. M. B. Holt, T. Stephenson, B. C. Olsen and D. Mitlin, *Energy Environ. Sci.*, 2013, **6**, 871-878.
46. Y. P. Wu, C. Y. Jiang, C. R. Wan, S. B. Fang and Y. Y. Jiang, *J. Appl. Polym. Sci.*, 2000, **77**, 1735-1741.
47. L. Qie, W.-M. Chen, Z.-H. Wang, Q.-G. Shao, X. Li, L.-X. Yuan, X.-L. Hu, W.-X. Zhang and Y.-H. Huang, *Adv. Mater.*, 2012, **24**, 2047-2050.
48. N. A. Kaskhedikar and J. Maier, *Adv. Mater.*, 2009, **21**, 2664-2680.
49. B. Fang, M.-S. Kim, J. H. Kim, S. Lim and J.-S. Yu, *J. Mater. Chem.*, 2010, **20**, 10253-10259.
50. F. Su, X. S. Zhao, Y. Wang, J. Zeng, Z. Zhou and J. Y. Lee, *J. Phys. Chem. B*, 2005, **109**, 20200-20206.
51. Z.-S. Wu, W. Ren, L. Xu, F. Li and H.-M. Cheng, *ACS Nano*, 2011, **5**, 5463-5471.
52. Y. Wang, F. Su, C. D. Wood, J. Y. Lee and X. S. Zhao, *Ind. Eng. Chem. Res.*, 2008, **47**, 2294-2300.
53. Y.-G. Guo, J.-S. Hu and L.-J. Wan, *Adv. Mater.*, 2008, **20**, 2878-2887.